Short communication

Three-dimensional thermal finite element modeling of lithium-ion battery in thermal abuse application

Guifang Guo[a], Bo Long[b], Bo Cheng[c], Shiqiong Zhou[a], Peng Xu[a], Binggang Cao[a,*]

[a] School of Mechanical Engineering, Xi'an Jiaotong University, 28#, Xian'ning West Road, Xi'an 710049, China
[b] School of Mechatronics Engineering, University of Electronic Science and Technology, Cheng'du 610054, China
[c] School of Construction Machinery, Chang'an University, Xi'an 710064, China

ARTICLE INFO

ABSTRACT

In order to better understand the thermal abuse behavior of high capacities and large power lithium-ion batteries for electric vehicle application, a three-dimensional thermal model has been developed for analyzing the temperature distribution under abuse conditions. The model takes into account the effects of heat generation, internal conduction and convection, and external heat dissipation to predict the temperature distribution in a battery. Three-dimensional model also considers the geometrical features to simulate oven test, which are significant in larger cells for electric vehicle application. The model predictions are compared to oven test results for VLP 50/62/100S-Fe (3.2 V/55 Ah) LiFePO$_4$/graphite cells and shown to be in great agreement.

© 2009 Elsevier B.V. All rights reserved.

1. Introduction

The environmental concern for air quality has spurred worldwide interest in the development of advanced batteries for electric vehicle propulsion application. Lithium-ion batteries are the state-of-the-art power sources for the electric vehicle. They combine excellent great cycle life, no memory effect, and high energy density. Development of lithium-ion batteries with large capacity and high power has been advanced for application to EV. With an increasing interest in large-format lithium-ion batteries for EV applications, one of the most important safety considerations for lithium-ion cells is thermal stability under various abuses such as exposure to overheating and external short-circuit. Therefore, the research of the thermal abuse tolerance is essential for large-scale batteries applications.

Thermal stability is a very important problem for cell safety. Several exothermic reactions occur inside a cell as its temperature increases. They may cause heat to accumulate inside the cells and accelerate the reactions between cells components if heat transfer from the cells to the surroundings is not sufficient. It will cause cell temperature to rise significantly, thereby risking thermal runaway if heat generation rate exceeds thermal dissipation rate. The balance between heat generation and dissipation rates is shown in Fig. 1. It is generally considered that thermal runaway occurs if T

is higher than T_1. T_1 is called the onset of thermal runaway (OTR) point, and T_2 is the fire point [1].

Researchers have tried to model the abuse reactions that occur in lithium-ion batteries [1–3]. Models available in the literature vary from relatively simple one-dimensional thermal models [4–8], considering radiation heat transfer and inner short-circuit behavior, to comprehensive three-dimensional models with non-isothermal, temperature dependent thermophysical properties and heat generation rates [9–11]. These models describe in detail the heat effects and the thermodynamic properties of battery materials and parts [12]. However, most of these papers are limited to cylindrical cells which are assembled using LiCoO$_2$ cathode, rather than newly LiFePO$_4$ cathode active materials and the normal capacity of cells is low less than 3 Ah and packs less than 150 Wh. Little research has been focused on the thermal abuse behavior of the large capacity and high power cells. Larger cells are more sensible to thermal runaway because they have higher energy content. Increasing cell size lowers cooling area per volumetric heat generation and increases thermal diffusion resistance. Therefore, thermal abuse performances of lithium-ion batteries with high capacity needed for electric vehicle application remains a great challenge.

In this study, a finite element method was used to develop the three-dimensional thermal abuse model on lithium-ion batteries. The model coupled with electrochemical reaction and thermal response to study in detail the temperature field distribution and evolution inside cell. A combination of experimental and thermal modeling was considered to evaluate the performance of lithium-ion cells under thermal abuse condition.

---

* Corresponding author. Fax: +86 029 82668835.
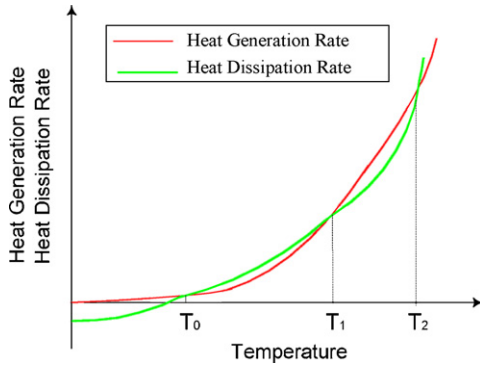E-mail address: cbg@mail.xjtu.edu.cn (B. Cao).

Fig. 1. The balance between heat generation rates and heat dissipation rates.

2. Model development

2.1. Calculation of temperature field

Assumed the initial temperature of the cell is θ (x, y, z), the boundary condition is conduction, convection, radiation and the known ambient temperature. The energy conservation equation is given as follows:

$$\rho C \frac{\partial \theta}{\partial t} = \frac{\partial}{\partial x}\left(k_x \frac{\partial \theta}{\partial x}\right) + \frac{\partial}{\partial y}\left(k_y \frac{\partial \theta}{\partial y}\right) + \frac{\partial}{\partial z}\left(k_z \frac{\partial \theta}{\partial z}\right) + q^B \quad (1)$$

where ρ and C are average density and average specific heat, respectively; K_x is the effective thermal conductivity along the direction perpendicular to a cell, while K_y and K_z are the effective thermal conductivities in the width and height directions of the cell. q^B denotes heat flow rate per unit area, that is, heat generation rate per unit volume.

The natural boundary condition:

(1) on the convection boundary is $\quad k_n \frac{\partial \theta}{\partial n} = h(\theta_e - \theta^s) \quad (2)$

where h is the convection coefficient on the temperature; θ_e is average temperature value and θ^s denotes surface temperature.

(2) on the radiation boundary is $\quad k_n \frac{\partial \theta}{\partial n} = k(\theta_r - \theta^s) \quad (3)$

where k and θ_r are radiation coefficient and the radiation flow temperature, respectively.

(3) on the heat transfer flux boundary is $\quad k_n \frac{\partial \theta}{\partial n} = q_{Sz} \quad (4)$

Also, the initial condition is $\quad \theta\big|_{t=0} = \theta(x, y, z) \quad (5)$

But, it is almost impossible that the solution on the differential equation according to the boundary value by employing function derivation. The finite element method is very effective method.

The above-mentioned differential equation used the variation calculus to establish functional transformation π, π function can be obtained as follows:

$$\pi = \int_V \frac{1}{2}\left\{ k_x\left(\frac{\partial \theta}{\partial x}\right)^2 + k_y\left(\frac{\partial \theta}{\partial y}\right)^2 + k_z\left(\frac{\partial \theta}{\partial z}\right)^2 \right\} dV - \int_{Sc} h\left(\theta_e \theta^s - \frac{1}{2}\theta^{s2}\right) dS$$
$$- \int_{Sc} \varepsilon f \sigma\left(\theta_r^4 \theta^s - \frac{1}{5}\theta^{s5}\right) dS - \int S_z \theta^s q_{Sz} dS - \int_V \theta q^B dV \quad (6)$$

where ε is emissivity, the value is between 0 and 1. σ is Stefan–Boltzmann constant, and $\sigma = 5.67 \times 10^{-8}\,\mathrm{w\,m^{-2}\,k^{-4}}$, f is the form factor of the radiant surface.

Selected first order difference of π function is zero and the equation can be written as:

$$\delta\pi = \int_V \delta(\underline{\theta}')^T \underline{K}(\underline{\theta}')dV - \int_{sc} h(\theta_e - \theta^s)\delta\theta^s dS - \int_{Sr} k(\theta_r - \theta^s)\delta\theta^s dS$$
$$- \int_{Sz} q_{Sz}\delta\theta^s dS - \int_V q^B \delta\theta dV = 0 \quad (7)$$

where $\quad (\underline{\theta}')^T = \left[\frac{\partial \theta}{\partial x} \frac{\partial \theta}{\partial y} \frac{\partial \theta}{\partial z}\right]$

$$\underline{K} = \begin{bmatrix} k_x & 0 & 0 \\ 0 & k_y & 0 \\ 0 & 0 & k_z \end{bmatrix}$$

It is essential for the finite element method that the overall temperature field function θ (x, y, z, t) changed to the temperature field function of all elements. So, one element functional variation equation can be obtained as follows:

$$\delta\pi_e = \delta(\underline{\theta}^e)^T\,{}^e\underline{K}^K\underline{\theta}^e - \delta\underline{\theta}^{sT}\underline{R}_s - \delta\underline{\theta}^T\underline{R}_B + \delta\underline{\theta}^T\,{}^e\underline{C}\underline{\theta}$$
$$- \delta\underline{\theta}^{sT}\,{}^e\underline{K}^C(\theta_e - \underline{\theta}^s) - \delta\underline{\theta}^{sT}\,{}^e\underline{K}^r(\theta_r - \underline{\theta}^s) \quad (8)$$

And $\delta\pi = \sum_{e=1}^{N} \delta\pi_e = 0$

The general heat flow balanced equation of the finite element system can be achieved

$$\underline{K}^K\underline{\theta} = \underline{Q}_S + \underline{Q}_B - \underline{C}\underline{\theta} + \underline{K}^C(\theta_e - \underline{\theta}^S) + \underline{K}^r(\theta_r - \underline{\theta}^S) \quad (9)$$

where $\underline{K}^K, \underline{C}, \underline{K}^C$ and $\underline{K}^r$ denote the general stiffness matrix, the total heat capacity matrix, the overall convection matrix and the general radiation matrix, respectively; $\underline{Q}_S$ indicates the heat flow vector of total nodes from the boundary heat source; $\underline{Q}_B$ represents heat flow vector of the total nodes occur in the inner heat generation.

Therefore, the above equations can be written as

$$[C]\{\dot{T}\} + [K]\{T\} = [Q] \quad (10)$$

where $[C]$ is the global thermal capacity matrix; $[K]$ denotes the global matrix of heat conduction; $\{T\}$ represents the global nodal temperature array; and $[Q]$ is the global temperature load array.

As we all know that the transition temperature distribution is the function of space and time, the solution field has been divided into the finite element meshes in order to solve the temperature function of elements. As a result, the solution of differential equation can be simplified by the numerical solution of algebraic equation.

2.2. Description of the model

Three sources of heat generation considered in the analysis of thermal runaway:

(1) The chemical reaction of the cell was called the "reversible" heat.
(2) The heat effects of ohmic resistance and polarization called "irreversible.
(3) The heat generated by "side reactions", for example, corrosion reaction, overcharge, and chemical shorts.

To develop a mathematical model that describes the heat abuse process, it treats the cell as a thermally homogenous body with effective thermophysical properties. The heat generation rates as
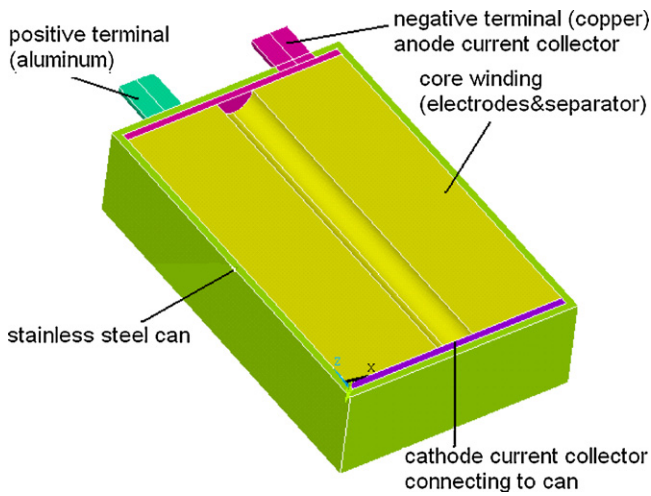
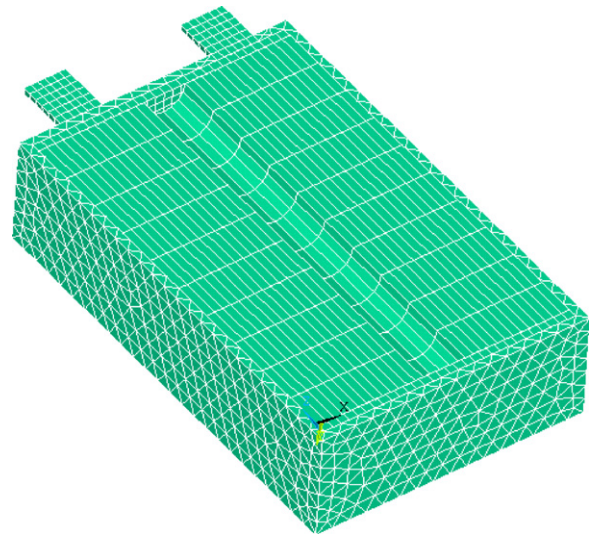Fig. 2. Schematic of the geometric model.

Fig. 3. Finite element model of lithium-ion cell.

input load in the simulation are estimated from experimental measurements depending temperature [13].

The total heat generation of the cell was determined as follows:

$$Q = Q_{irrev} + Q_{rev} = \Delta G + T\Delta S + W_{el}$$
$$\Delta G = -nFE_{eq}$$
$$\Delta S = nF\frac{dE_{eq}}{dT} \tag{11}$$
$$W_{el} = -nFE$$

$$Q_{rev} = T\Delta S = \left(\frac{\partial E_{eq}}{\partial T}\right)(It) \tag{12}$$

The heat generation rate was calculated:

$$q_{rev} = \frac{\partial Q_{rev}}{\partial t} = IT\left(\frac{\partial E_{eq}}{\partial T}\right) \tag{13}$$

$$Q' = q_{irrev} + q_{rev} = I\left[(E_{eq} - E) + T\frac{dE_{eq}}{dT}\right] \tag{14}$$

Eq. (14) is the sum of the reversible and the irreversible heat effects, while the entropy term was estimated from the measured experimentally as described in [14].

Aiming at the electric heating field characters of the cell, the model employed three-dimensional heat transfer elements, heat transfer coupled with electrically conductive elements and heat convection surface elements to carry out the heat conduction, convection and heat generation as inputs in the simulation calculations.

Fig. 2 shows a schematic of sample model geometry. A half model with geometrical symmetry is created. The geometric model includes the cell component details such as aluminum/copper current collectors and terminals, insulator block, stainless steel container, and cell core winding. Moreover, the container can is electrically and thermally connected to one of the terminals.

The computational mesh used in the simulations is divided as shown in Fig. 3 in order to ensure the calculation accuracy and save

on computing time. There are 145,086 elements and 27,149 nodes in the thermal analysis.

3. Experimental

The lithium-ion cell used in the investigation was VLP 50/62/100S-Fe (3.2 V/55 Ah) LiFePO$_4$/graphite cells. The nominal cell capacity was 55 Ah, the dimension (thickness × width × length) was 50 mm × 62 mm × 100 mm. Cathodes and anodes were coated on aluminum and copper foils, respectively. Both electrodes used PVDF and NMP binder. The separator was made of tri-layers of polypropylene, polyethylene and polypropylene (PP/PE/PP). The electrolyte consisted of 1 M LiPF$_6$ in ethylene carbonate (EC)–dimethyl carbonate (DMC)–ethyl methyl carbonate (EMC) (1:1:1, mass ratio) electrolyte. The parameters of lithium-ion cell for model calculations are listed in Table 1 [15–17].

A press gauge was placed at the vent to monitor the internal pressure change during the tests. The thermocouples (type T, 2 mm diameter) were used to measure internal and external temperatures response during thermal abuse reactions. The cell containing internal thermocouples had the thermocouple inserted into the wound element stack and the external thermocouple was attached to the surface center of the cell.

The cell was initially at a normal operating temperature, that is 25 °C, and was charged first in galvanostatic mode at 1 C rate with a voltage cut-off limit of 4.2 V and then in a potentiostatic mode until the current dropped to 1000 mA. After 2 h stewing, the cell was then suddenly placed in an oven that was preheated to the desired test temperature. The oven temperature was kept constant during the test. The heat generation in a cell includes the contributions from entropy change, ohmic heating, and electrochemical polarization. The thermal boundary condition for the cell exterior surface is that natural convection and radiation heat transfer are calculated, $h = 8.7$ W m^{-2} K and $\varepsilon = 0.8$. Tests were carried out on cells at oven temperature ranging from 140 °C to 160 °C.

Table 1
Thermal-physical properties parameters of materials.

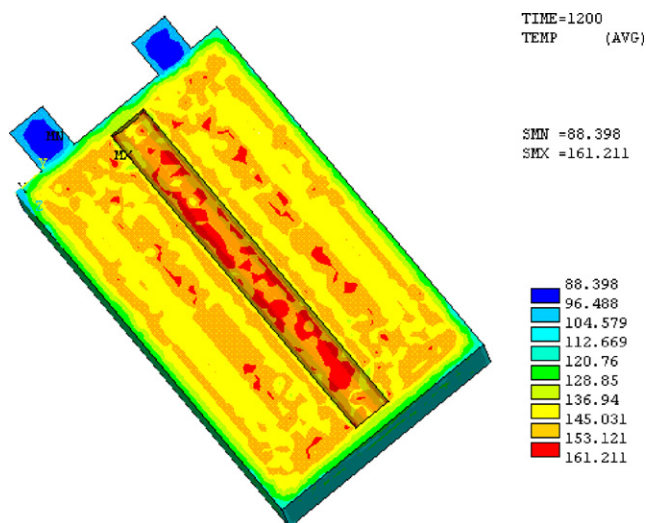| Parameter	Electrolyte	Separator	Positive plate		Negative plate		Container
	LiPF$_6$/EC + DMC + EMC	PP/PE/PP	LiFePO$_4$	Aluminum	Graphite	Copper	1Cr18Ni9Ti
ρ (kg m^{-3})	1290	492	1500	2700	2660	8900	7800
C_o (J kg^{-1} K^{-1})	133.9	1978	1260.2	903	1437.4	385	460
K (W m^{-1} K^{-1})	0.45	0.334	1.48	238	1.04	398	66.6

Fig. 4. The contours of temperature for the cell in oven test at 155 °C at 1200 s.

Moreover, the capacity of cells was compared before and after test.

4. Results and discussion

The cells used in the oven test were charged at C/3 and discharged at 1 C rate. The cells showed high capacity characteristic even at elevated temperature. The average discharge capacities were 96.12% and 93.48% of the rated capacities under 140 °C and 150 °C. The test results and simulation results of the temperature fields are very close. In other word, the qualitative, quantitative analysis and whether or not the cell will go to thermal runaway are also predicted accurately.

The contours of temperature for the cell oven test at 155 °C at 1200 s, 3600 s are presented in Figs. 4 and 5, respectively.

From Fig. 4, it is seen that the temperature distribution of the cell in oven test at 155 °C at 1200 s is non-uniform. The non-uniform distribution affects the results that heat exchange between the cell and ambient environment is more accurately calculated and heat generation variation can also be evaluated more accurately. As the cell heats up, the temperature is highest at the can surface and decreases toward the core. As the exothermic reactions are acti-
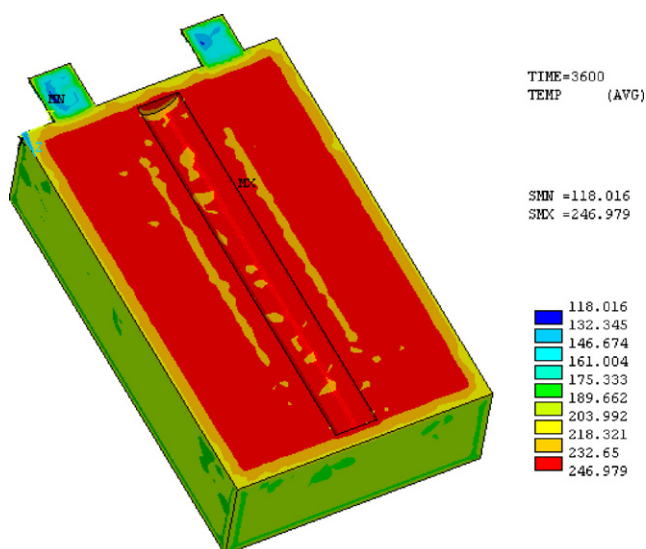

Fig. 5. The contours of temperature for the cell in oven test at 155 °C at 3600 s.
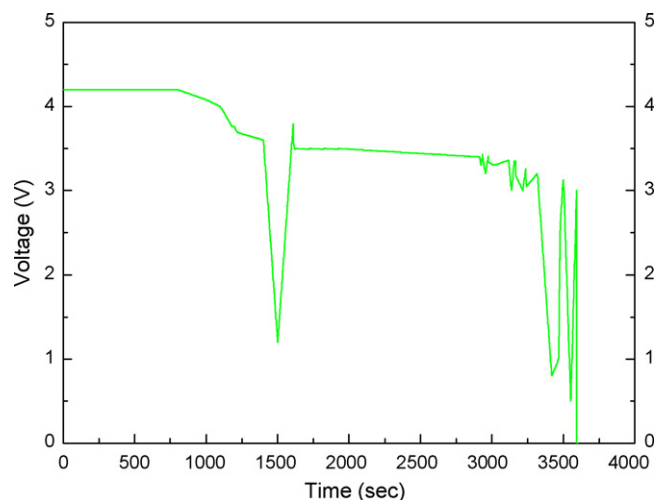

Fig. 6. The voltage profile of the cell during the 155 °C oven test.

vated and start to release heat, the interior temperature of the cell increases, and the temperature reaches a maximum at the center. Since the heat generation is much larger than the surface heat reaction, the temperature distribution is dominated by the heat generation.

As shown in Fig. 5, above 246 °C, the cell undergoes thermal runaway at about 3600 s. The highest temperature appears at the cell center. The temperature distribution non-uniformity is more apparent and the temperature gradient is larger. At this stage, the possible exothermic reactions are: (1) the chemical reduction of the electrolyte by the anode; (2) the thermal decomposition of the electrolyte; (3) the oxidation of the electrolyte on the cathode; (4) the thermal decomposition of the anode; (5) the thermal decomposition of the cathode. This is mainly because the metastable components of the SEI decompose getting faster and faster. The lithium ions remaining in the cathode are removed and more lithium ions are inserted in the carbon. In addition, as the temperature increases, there are further exothermic decompositions, including the electrolyte decomposition, and the melting of lithium will lead to a strong exothermic reaction with electrolyte. As well known, it may be the key factors which result in the thermal runaway of cell that occur the exothermic reaction of $LiFePO_4$ achieved in this test and give off oxygen that can react exothermically strong with the electrolyte. In fact, does the reaction of cathode occur?

Fig. 6 shows the cell voltage variations during the 155 °C oven test.

It is clear that the $LiFePO_4$ has excellent thermal stability in the cell. Around at 1200 s, the cell voltage dropped quickly to 1.3 V and then suddenly recovered to 3.6 V. After the cell voltage had recovered, it remained at an almost constant value during the heating test until the voltage sharp decreased to 0 once more caused by internal short-circuit induced the thermal runaway may occur [18]. The results indicate that $LiFePO_4$ active material is more thermally stable under oxidation potential than $LiCoO_2$ as reported in [19].

Fig. 7 shows the cell temperature variations for four oven temperature cases. Internal heat generation resulted from thermal abuse reactions. The cells placed in the 140 °C and 150 °C oven test do not go into thermal runaway, while the cell heating in the oven at 155 °C and 160 °C goes into thermal runaway. In the 155 °C and 160 °C oven heating cases, heat generation rapidly increased to exceed the heat dissipation to ambient at about 60 min and 50 min and led to thermal runaway, respectively. Because of the relatively higher oven temperature (160 °C), the cell heats rapidly, the thermal runaway is advanced by several minutes in the
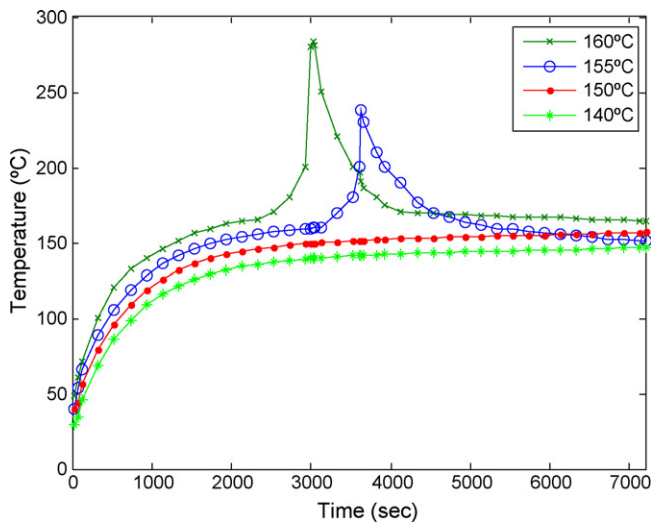
Fig. 7. Comparison of simulation of effect of oven temperature on thermal response.

Fig. 8. Comparison of model prediction and oven test data at 155 °C.

three-dimensional simulation compared to the thermal response of 155 °C oven test.

This thermal runaway behavior has been explained that at about 100 °C, the metastable components of the solid electrolyte interphase (SEI) at the anode decompose very rapidly. Therefore, the metastable SEI form to stable SEI and exothermal reactions occur. This provides an exothermic peak boost to the remaining reactants in the cell as proposed in [20]. The mechanism of reactions may be as follows:

$$(CH_2OCO_2Li)_2 - Li_2CO_3 + C_2H_4 + 1/2O_2 \quad \text{or}$$

$$2Li + (CH_2OCO_2Li)_2 - 2Li_2CO_3 + C_2H_4$$
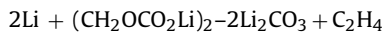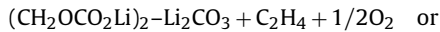
Therefore, above 100 °C, the first temperature increase is due to SEI formed at the anode. At about 143 °C, the large temperature increase is because of PP/PE/PP separator shutdown mechanism in the microporous separator membrane present in the Li-ion cells. The pores of separator collapse to the form of a relatively non-porous insulating film between the anode and the cathode [21–24]. Consequently, the cell placed in the 140 °C and 150 °C oven test is safer. However, at temperature higher than 150 °C, the separators meltdown and the pinholes formed in non-porous film it is possible to lead to an internal short-circuit. Moreover, the large amount of side reactions exothermal heat generation will induce the cells go into thermal runaway.

Fig. 8 indicates the comparison for model prediction results and actual oven tests on lithium-ion cells. From the figure it is clear that the model predicts the qualitative behavior of a cell in the oven test very well. However, there are some deviations from model predictions in the oven test data. First, the exact time of thermal runaway is not predicted very well. This is due to the simple fact that the safety vent on the cell opens, electrolyte vapor is released, producing coolness by the Joule-Thompson effect in the actual cell that is unable to be included in the model. The other major difference between the mode and the oven tests is the maximum temperature reached by the cell. The maximum temperature of the oven test data is lower. In general, the model simulation results generally matched with the oven test results.

The temperature gradient predicted inside the cell is shown in Figs. 9–11 for 55 Ah cell under 150 °C. Simulation results demonstrate that the temperature gradient along X(thickness)-direction is the highest, while the temperature gradients in Y(width)-direction are small and similar characteristics exist in Z(length)-direction at the end of oven test. The cell center temperature is about
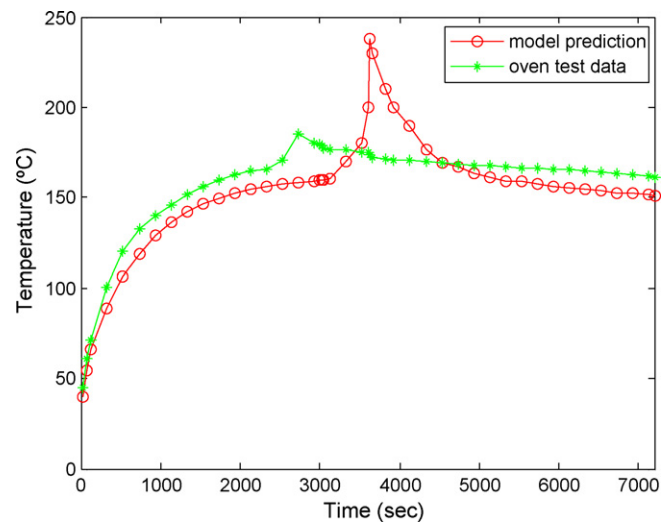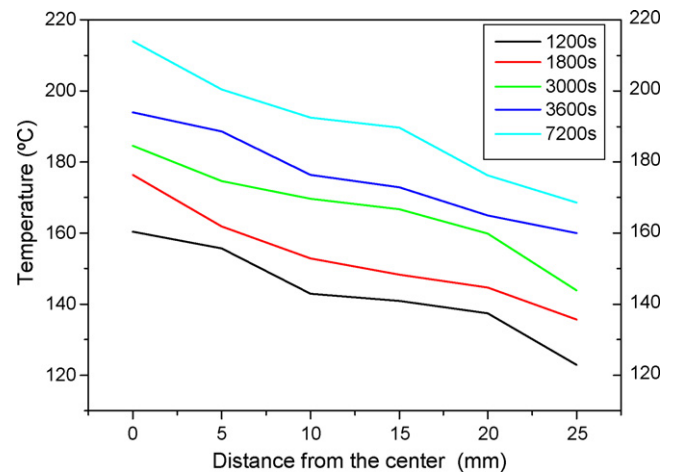

Fig. 9. Simulated temperature profile along the X (thickness)-direction at different times.
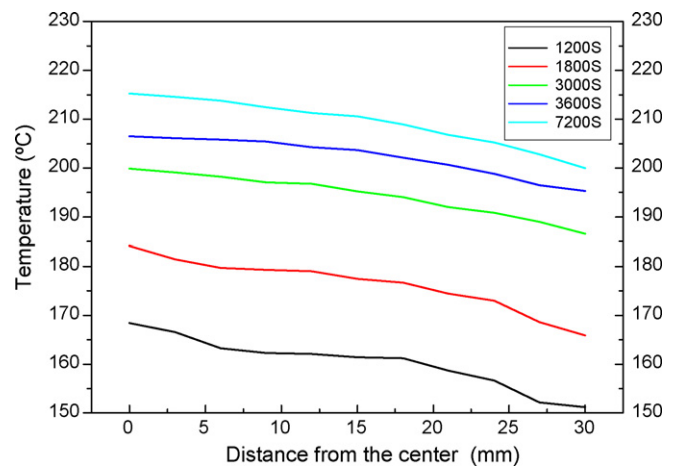

Fig. 10. Simulated temperature profile along the Y (width)-direction at different times.

30 °C higher than the surface temperature along X-direction. The insignificant effects resulting from the heat transfer resistance in X-direction may be very large followed by different material with small thermal conductivity. That is, the relatively large thermal con-
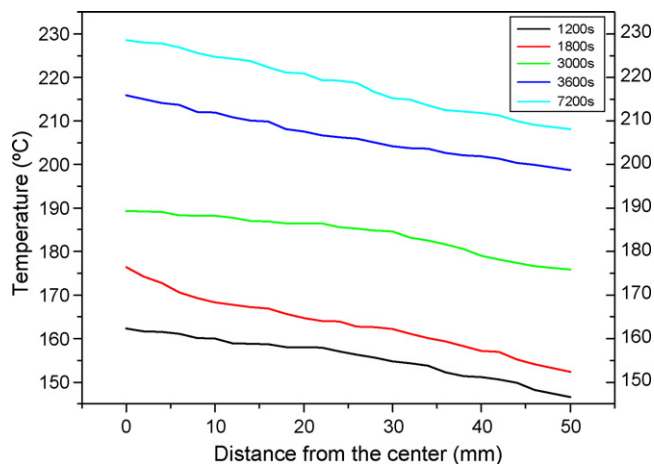
Fig. 11. Simulated temperature profile along the *Z* (length)-direction at different times.

ductivity along the *Y* and *Z* directions allows heat to be removed from the cell. Therefore, the steep temperature variation inside cell results from the difference in heat transfer efficiency in cell. This is in agreement with the results given by [2,25].

5. Conclusion

A finite element method was used to develop the three-dimensional thermal abuse model on the high capacity of lithium-ion batteries. Oven test simulation indicates the non-uniform temperature distribution in the three-dimensional cell. Moreover, the model predicts the qualitative and the quantitative behavior of a cell in an oven test very well, and whether or not the cell will go to thermal runaway is also predicted accurately. The model predictions are compared to oven test results and shown to be in great agreement. The results indicate that the LiFePO$_4$ active material is more thermally stable under oxidation potential than LiCoO$_2$. These safety characteristics of the LiFePO$_4$ cathode are very attractive with respect to large cells. Application of high thermal stability materials and slowing down the active materials' thermal reactions are potential strategies to protect lithium-ion cells from thermal runaway. Furthermore, the shutdown mechanism of the separators can improve cell safety during abuse test, so addition of the ceramic coating's should contribute to the strength and resis-tance to melting and shrinking of the separator. This will be very significant that protects thermal runaway of the larger lithium-ion battery because larger cells are sensible to thermal runaway.

Moreover, it was found that there is little temperature gradient (about difference between center and surface) along width and length direction inside the cell geometry when placed in150 °C oven test, while the maximum of the temperature gradient along thickness. The small temperature gradient suggests that the relatively large thermal conductivity along the *Y* and *Z* directions allows heat to be removed from the cell. Therefore, the three-dimension model will be more powerful and flexible in simulating the thermal performance of batteries with different parameters and assisting the design of thermal management systems.

References

[1] J. Lee, K.W. Choi, N.P. Yao, C.C. Christianson, J. Electrochem. Soc. 133 (7) (1986) 1286–1291.
[2] Y. Chen, J.W. Evans, J. Electrochem. Soc. 140 (7) (1993) 1833–1838.
[3] T.D. Hatchard, D.D. MacNeil, A. Basu, J.R. Dahn, J. Electrochem. Soc. 148 (7) (2001) A755–A761.
[4] S.A. Hallaj, H. Maleki, J.S. Hong, J.R. Selman, J. Power Sources 83 (1) (1999) 1–8.
[5] T.D. Hatchard, D.D. MacNeil, D.A. Stevens, L. Christensen, J.R. Dahn, J. Electrochem. Solid-State Lett. 3 (7) (2000) 305–308.
[6] T. Yamauchi, K. Mizushima, Y. Satoh, S. Yamada, J. Power Sources 136 (1) (2004) 99–107.
[7] R. Spotnitz, J. Franklin, J. Power Sources 113 (1) (2003) 81–100.
[8] R.M. Spotnitz, J. Weaver, G. Yeduvaka, D.H. Doughty, E.P. Roth, J. Power Sources 163 (2) (2007) 1080–1086.
[9] S.C. Chen, C.C. Wan, Y.Y. Wang, J. Power Sources 140 (1) (2005) 111–124.
[10] S.C. Chen, Y.Y. Wang, C.C. Wan, J. Electrochem. Soc. 153 (4) (2006) A637–A648.
[11] G. Kim, A. Pesaran, R. Spotnitz, J. Power Sources 170 (2) (2007) 476–489.
[12] S. Tobishima, J. Yamaki, J. Power Sources 81–82 (1999) 882–886.
[13] K. Takano, Y. Saito, K. Kanari, J. Appl. Electrochem. 32 (2002) 251–258.
[14] E.P. Roth, D.H. Doughty, J. Power Sources 128 (2004) 308–318.
[15] A.M. Collieu, D.J. Powney, The Mechanical and Thermal Properties of Materials [M], Edward Arnold (1973).
[16] Q.F. Ma, R.S. Fang, Thermophysical Properties of Engineering Material' Handbook [M], China Machine Press, 1986.
[17] Y. Zhao, Y. Bai, X.J. Liu, J. Power Technol. 132 (7) (2008) 461–463.
[18] M. Takahashi, H. Ohtsuka, K. Akuto, J. Electrochem. Soc. 152 (2005) A899–A904.
[19] D.D. MacNeil, L. Christensen, J. Landucci, J.M. Paulsen, J. Electrochem. Soc. 147 (2000) 970–979.
[20] M.N. Richard, J.R. Dahn, J. Electrochem. Soc. 146 (6) (1999) 2068–2077.
[21] X. Liu, H. Kusawake, S. Kuwajima, J. Power Sources 97–98 (2001) 661.
[22] F.C. Laman, M.A. Gee, J. Denovan, J. Electrochem. Soc. 140 (1993) L51.
[23] A.J. Bradley, R.E. White, J. Power Sources 70 (1998) 48.
[24] G. Venugopal, J. Moore, J. Howard, S. Pendalwar, J. Power Sources 77 (1999) 34.
[25] K. Kanari, K. Takaro, Y. Stito, Proceedings of International Workshop on Advanced Batteries, Japan, IC07, in Japanese, 1998, p. 217.